THE UNIVERSITY OF CHICAGO

CONSTRAINTS ON CLUSTER STRUCTURE AND COSMOLOGY FROM A COMPARISON OF X-RAY AND SUNYAEV-ZEL'DOVICH EFFECT PROPERTIES IN GALAXY CLUSTERS

A DISSERTATION SUBMITTED TO
THE FACULTY OF THE DIVISION OF THE PHYSICAL SCIENCES
IN CANDIDACY FOR THE DEGREE OF
DOCTOR OF PHILOSOPHY

DEPARTMENT OF ASTRONOMY & ASTROPHYSICS

BY
SAMUEL J. LAROQUE

CHICAGO, ILLINOIS
JULY 10, 2005

To Mom and Ed.

ABSTRACT

We present a study of 36 massive galaxy clusters at redshifts $0.14 \leq z \leq 0.89$, whose properties are used to constrain cluster structure and cosmological models. The clusters are studied at both X-ray wavelengths using data from the *Chandra X-ray Observatory*, and at centimeter wavelengths using Sunyaev-Zel'dovich Effect (SZE) data from the BIMA and OVRO interferometric arrays. Likelihood analysis is performed using a Markov chain Monte Carlo (MCMC) method, and we motivate and adopt an isothermal β-model with central 100 kpc excluded from the X-ray data to describe the intracluster medium in all 36 clusters. This model is shown to provide consistently good fits to clusters with a wide range of morphological properties. Best-fit cluster gas masses, total masses, and integrated SZE fluxes are determined from this model within the MCMC framework. X-ray and SZE results are then used in an effort to constrain cluster structure and cosmology. First, the integrated SZE flux is compared with X-ray derived gas mass, spectroscopic temperature, and total mass to determine how firmly connections between observables and derived cluster properties can be established in SZE surveys. These properties are found to display tight scaling relations over the full range of redshift. Cluster gas mass fractions from both X-ray and SZE data are then compared, and the implications for cluster structure are noted. The gas mass fractions are used to obtain constraints on Ω_M and Ω_Λ both by comparing the mean $f_{\rm gas}$ values to Ω_B/Ω_M for assumed Ω_B, and by assuming that $f_{\rm gas}$ should be constant with redshift and determining what cosmology best facilitates this. Cosmological constraints are found to be consistent with CMB results, but a better understanding of the cluster baryon budget is needed to achieve the same level of precision.

ACKNOWLEDGMENTS

I must start by thanking my advisor, John Carlstrom, who in Spring 1999 plucked me out of first year obscurity and threw me into the lab to work on the *DASI* experiment. I never looked back. John has been patient and generous with me through the years, even opening up his home to me so that I could wrap up my thesis in Chicago. Thank you John, for your support, and much thanks also to Mary, Will, Alice and Sally for your generosity and making my days in Chicago this past year so comfortable.

Marshall Joy has often been like a second advisor to me, providing an additional point of view and being a trusted confidant. He has always helped me to see the positive side of things, even on the bad days, and his guidance has always come with a large dose of patience, which I have greatly appreciated. I have learned a tremendous amount from Marshall, both about science and about life in general, and I will carry his many insights forward with me.

Many others have provided invaluable assistance in my thesis project. Most notably I thank Max Bonamente and Daisuke Nagai. Max taught me virtually everything I know about X-ray astronomy and has always been happy to talk over the most minor of details. He has a remarkable ability to make what might otherwise seem boring and tedious feel fun. Daisuke, with whom I shared an office for the past four years, has always been available to provide the theoretical viewpoint on issues, and seems to have a satisfactory answer for just about any question put to him. I have learned a tremendous amount about the theoretical underpinnings of cluster formation and evolution through what must number hundreds of hours of conversation with Daisuke, and I count him among my closest friends.

My career as a graduate student has not been confined to the workplace, thank goodness, and there are many people in my personal life without whom this would not have happened. First and foremost I thank my mother and my stepfather, Miriam and Ed Landesman, for their unflagging support and encouragement. They were always there to pick me up when I felt down and to remind me that I could, indeed, do this. And they were right. My girlfriend of the past four years, Christy Hagan, has also provided unwavering support. She has stuck right by me through both the highs and lows of my research and writing. Her love and support have been just as important as her bottomless patience with me. Brian Wilhite, who has played the roles of classmate, roommate, and close friend, also helped smooth the occasionally rough edges of graduate school. Life with him on the "hipper, trendier" North Side was an experience I will never forget, and I will always value his friendship. My father and stepmother, Robert and Gail LaRoque, have always been there for me too, encouraging me to reach a little higher. Their advice and encouragement has paid off. And finally, my sister Elly has always set examples for me through her hard work and perseverance. Bringing out the best in all those around her, she has served as a great inspiration for me.

Others who made this project happen include Nils Halverson, who got me up to speed in the lab working on the DASI receivers in my first research project as a graduate student. Erik Reese filled a similar role in the office, instructing me in the finer details of the Sunyaev-Zel'dovich effect and guiding me through my first serious research. Kyle Dawson, a close friend since college, made observing that much more fun. In addition to taking me on some pretty hairy bike rides, he has taught me much about interferometry and the CMB. Erik Leitch always had an open door policy to discuss just about anything, from window functions to the Roman Empire, and I enjoyed his friendship through the years. Carlo Graziani has always been available to talk statistics. And of course much thanks is due to the people at the BIMA and OVRO observatories, including Rick Forster, Dick Plambeck, and Dave Woody, for helping make our observing runs so productive and enjoyable.

Beyond my research I thank Mark Hoffman for being a good friend and a great symphony buddy, and John Everett for his enthusiasm and friendship. Craig Tyler, along with Brian and John, helped me survive my first year here. Sandy Heinz made the transition from college to graduate school bearable, and remains to this day a patient listener and good friend. And I will never forget Melissa Minkov, who taught me to approach problems with a positive attitude and a smile. She is greatly missed.

Finally, thank you to NASA, who has supported this project and me directly through their Graduate Student Researchers Program (GSRP). On the Chicago end, Mary Wawro has always helped me navigate the bureaucracy of my fellowship. On the Huntsville end, Ed Jones and Marilyn Lewis-Alim were particularly helpful through the years.

TABLE OF CONTENTS

LIST OF FIGURES

LIST OF TABLES

CHAPTER 1

INTRODUCTION

Clusters of galaxies have for a long time been recognized as a valuable probe of cosmological models. With masses in excess of $10^{14}\,\mathrm{M}_{\odot}$ and diameters of several Mpc, they are the largest collapsed objects in the universe and their large sizes and distances provide various tests of cosmology. For example, there is no known way to segregate baryons from dark matter on the mass and size scales of galaxy clusters. The matter content in clusters is therefore expected to reflect the matter content of the universe as a whole, and provide constraints on the ratio of baryons to total matter, Ω_B/Ω_M (White et al., 1993b; Evrard, 1997). Using estimates of Ω_B obtained from Big Bang nucleosynthesis or studies of the cosmic microwave background, we can place constraints on Ω_M. An extension of this method allows constraints on Ω_Λ as well. The ratio of baryons to total matter in a cluster is expected to be constant with redshift, but determination of this ratio generally depends on cosmology through the angular diameter distance $D_{\rm A}$ to a cluster. Measurements of the mean baryonic mass fraction as a function of redshift can therefore constrain Ω_M and Ω_Λ through its $D_{\rm A}$ dependence (Sasaki, 1996; Pen, 1997). Clusters can also be used to obtain direct measurements of $D_{\rm A}$ by probing the Hubble flow out to high redshift. Measurements of the X-ray surface brightness $S_x \propto n_e^2 dl$ can be combined with measurements of the Sunyaev-Zel'dovich effect (SZE) $\Delta T \propto n_e dl$ to determine the length scale of a cluster. This, combined with the cluster's redshift, can be used to determine $D_{\rm A}$, and when averaged over a large sample this provides an independent measurement of the Hubble constant H_0, free of distance-ladder calibration systematics (Birkinshaw et al., 1991; Reese et al., 2002).

Clusters also provide valuable information about the large scale structure of the universe. Since the formation of cluster dark matter potential wells is thought to depend primarily on gravitational physics, the abundance of clusters and their redshift distribution should depend mainly on the geometry of the universe and power spectrum of initial density fluctuations. Probing this abundance to high redshift can therefore be used to constrain cosmological parameters such as Ω_M, Ω_Λ, σ_8, and even the equation of state of the dark energy w (e.g., White et al., 1993a; Bahcall & Fan, 1998; Viana & Liddle, 1999; Haiman et al., 2001). Current and upcoming surveys will search for cluster emission signatures at X-ray, microwave, and optical wavelengths (e.g., Romer et al., 2001; Holder et al., 2000b; Gladders & Yee, 2005) in an effort to compile large, well-selected cluster catalogs which can be used to constrain cosmological parameters.

An accurate determination of cosmological parameters using these methods relies on understanding systematic uncertainties associated with galaxy clusters. Past determinations of, e.g., Ω_M and H_0 relied on assumptions such as cluster isothermality and sphericity, and a smooth distribution of gas in the intracluster medium (Grego et al., 2001; Reese et al., 2002). Departures from these and other assumptions can lead to systematic offsets in the derived cosmological parameters. Cluster surveys are also highly sensitive to systematic uncertainties since they assume a certain degree of regularity in cluster structure to constrain cosmology (Haiman et al., 2001). The degree to which these assumptions hold must be understood to place realistic limits on cosmological parameters.

1.1 Thesis Goals and Structure

In this thesis, we present a sample of 36 massive galaxy clusters with both archival *Chandra* X-ray data and centimeter-wave interferometric SZE data. We perform a maximum likelihood analysis using a Markov chain Monte Carlo method to determine both the gas masses and total gravitational masses of the 36 clusters. The ratio of gas mass to total mass is used to determine Ω_M and Ω_Λ using the methods described above, and the results are compared with those of previous studies. In addition, we compare the integrated SZE flux of each cluster with its X-ray determined mass and temperature in an effort to better understand cluster regularity and our ability to constrain cosmology through SZE cluster surveys. All told, our results provide a better understanding of both cosmology and cluster structure and evolution, as well as associated systematic uncertainties.

Although optical tools such as deep optical surveys and gravitational lensing are valuable ways of studying clusters, in this thesis we focus only on X-ray and SZE methods. In Chapter 2, we describe the theoretical properties and observational history of both X-ray emission and the SZE in clusters. We then describe in detail the major cosmological tests that these datasets can provide and some of the problems encountered when interpreting the results of these tests. In Chapter 3 we describe the properties of the cluster sample used in this study. The X-ray and SZE observations and data reduction are summarized in Chapter 4. In Chapter 5 we explain the cluster models and analysis used to extract cosmological parameters from the data, and our results are presented in Chapter 6 along with their implications for cosmology and cluster physics. An assessment of major systematic uncertainties is also presented. Finally, our conclusions and discussion of future prospects are contained in Chapter 7. All uncertainties are at the 68.3% confidence level unless otherwise stated.

CHAPTER 2

X-RAYS AND SZE IN GALAXY CLUSTERS

Although galaxy clusters were first detected optically in the early twentieth century, the later discoveries of X-ray emission and most recently the SZE toward clusters has expanded our toolset for performing cosmological studies. Here we describe the history and physics of X-ray emission and the SZE in galaxy clusters, and describe some of the ways these emission mechanisms can be used to study clusters and cosmology.

2.1 X-ray Emission From Clusters

A detailed account of the history of cluster studies using X-ray data can be found in Sarazin (1988), but a brief overview is presented here. X-ray emission from clusters was first detected in 1966 in the direction of M87 in the Virgo cluster, followed by detections in the directions of Coma and Perseus. Launch of the *Uhuru* satellite in 1970 allowed a complete survey of the X-ray sky (Giacconi et al., 1972) and confirmed that galaxy clusters are the most common bright extragalactic sources. Further studies showed that cluster X-ray emission is extended and that clusters are among the most luminous X-ray sources in the universe, second only to quasars.

These discoveries gave rise to three main theories regarding the source of the X-ray emission. The first postulated that the emission came from inverse Compton scattering of cosmic microwave background (CMB) photons off a population of relativistic electrons in the cluster (Felten & Morrison, 1966). The scattering could be caused by the same electron population responsible for synchrotron emission already detected in clusters. The second theory attributed the X-ray emission to a large population of stellar X-ray sources such as those seen in our own galaxy (Katz, 1976). This could produce the observed X-ray emission if clusters had a ratio of X-ray luminosity to mass comparable to that observed in globular clusters. The third theory suggested that the emission arose from thermal bremsstrahlung emission associated with a diffuse ionized plasma permeating the cluster, having a temperature $T_{\rm gas} \sim 10^8$ K and density $n \sim 10^{-3}$ cm^{-3} (Felten et al., 1966). Studies showed that the cluster X-ray luminosity increased with the velocity dispersion of cluster galaxies, and that the cluster mass implied by the velocity dispersion was 10—100 times greater than that of the galaxies themselves. This supported the bremsstrahlung theory by suggesting that a roughly constant fraction of the total cluster mass could be in hot intracluster gas (Solinger & Tucker, 1972).

Launch of both the HEAO-1 satellite and the *Einstein Observatory* in the late 1970's helped to resolve these competing theories. HEAO-1's 2—60 keV spectral coverage led to detailed cluster spectra which showed that continuum emission fell off exponentially with energy. This was consistent with thermal bremsstrahlung but not with the power law shape expected from inverse Compton scattering. Furthermore, the spectra showed a complex of line emission around 7 keV thought to be associated with highly ionized iron. While consistent with thermal excitation in a hot intracluster gas, the inverse Compton and discrete source scenarios offered no explanation for line emission. The *Einstein Observatory* was the first X-ray instrument with focusing optics, allowing greatly improved angular resolution in X-ray imaging. The *Einstein* images showed no correlation between the X-ray and radio emitting regions of clusters as required by the inverse Compton emission, nor did they show the granularity of X-ray emission expected if discreet sources were the source. The images instead showed a very smooth distribution of gas (Jones & Forman, 1984), consistent with the thermal bremsstrahlung scenario. This, combined with the line emission and luminosity-velocity dispersion relation, essentially confirmed the thermal bremsstrahlung theory.

Subsequent X-ray missions with greater angular resolution and sensitivity, such as the*Röntgen Satellite* (*ROSAT*), and missions with improved spectral coverage and energy resolution, such as the *Advanced Satellite for Cosmology and Astrophysics* (*ASCA*) and *BeppoSAX*, have continued to study the intracluster gas. Most recently, the *Chandra X-ray Observatory* with its arcsecond angular resolution and the *XMM-Newton* mission with its high sensitivity, have shown that the gas has more structure than previously believed, containing hot diffuse regions and cool dense regions. Some implications of these findings will be addressed in our discussion of systematic uncertainties; in the meantime we examine thermal bremsstrahlung and several lesser contributions to cluster X-ray emission in more detail.

2.1.1 Thermal Bremsstrahlung

Bremsstrahlung, or free-free emission, is radiation due to acceleration of a charge in the Coulomb field of another charge. This is the dominant X-ray emission mechanism in the intracluster gas. We examine in particular electron-ion bremsstrahlung, since the low mass electrons dominate the radiation. Electrons in the gas are assumed to have a thermal velocity distribution, and the emissivity at frequency ν of a gas containing ions of charge Ze is given by (Rybicki & Lightman, 1979):

$$\epsilon_\nu^{ff} = \frac{2^5 \pi e^6}{3 m_e c^3} \left(\frac{2\pi}{3 k_{\rm B} m_e} \right)^{1/2} T_e^{-1/2} Z^2 n_e n_i e^{-h\nu/k_{\rm B} T_e} g_{ff}(Z, T_e, \nu) \tag{2.1}$$

where T_e is the electron temperature of the gas, n_i is the number density of ions, n_e is the number density of electrons, m_e is the electron mass, g_{ff} is a quantum correction known as the Gaunt factor, and the other constants have their usual values. The emissivity has cgs units of erg s^{-1} cm^{-3} Hz^{-1}. Additional, though much weaker, continuum processes include radiative recombination (free-bound) emission and two-photon decay processes, while line emission due to collisional excitation and radiative recombination contribute to the total emissivity as well. The emissivity from each of these processes is proportional to the electron and ion densities, so the total emissivity can be expressed as (e.g., Sarazin, 1988):

$$\epsilon_\nu = \Lambda_\nu n_i n_e \tag{2.2}$$

where Λ_ν, the emission per ion at unit electron density and frequency ν, is called the X-ray cooling function and incorporates the contributions from individual emission processes in the gas. In practice, the X-ray cooling function is usually integrated over the frequency band to which an instrument is sensitive and denoted simply Λ. When Eq. [2.1] is integrated over frequency, the temperature dependence becomes $T_e^{1/2}$ instead of $T_e^{-1/2}$; furthermore the ion and electron densities are trivially related by the mean molecular weight of the gas. In the frequency bands typically used to study clusters, bremsstrahlung is the primary emission process for temperatures $T_e \gtrsim 3$ keV. The temperature dependence of the cooling function therefore works out to $\Lambda \propto n_e^2 T_e^{1/2}$, a relation which will be revisited frequently. Several codes exist to determine Λ given a temperature, elemental abundance, and frequency band, such as those of Raymond & Smith (1977) and Mewe et al. (1985). A model X-ray emission spectrum, showing emissivity as a function of energy, is shown in Figure 2.1. This spectrum, generated with the Raymond & Smith (1977) code, corresponds to an isothermal cluster at redshift $z = 0$ with $T_e = 10$ keV and elemental abundance equal to 30% of the solar values. The energy range shown, 0.3—10 keV, is typical of the *Chandra* ACIS detector.

The X-ray emissivity is not a directly observable quantity; instead X-ray proportional counters measure the X-ray surface brightness over some frequency band,

$$S_x = \frac{1}{4\pi(1+z)^4}\int n_e n_{\mathrm{H}} \Lambda \, d\ell \tag{2.3}$$

where the integral is along the line of sight and typical cgs physical units are erg cm^{-2} ster^{-1} s^{-1}. Given sufficient angular resolution, the X-ray surface brightness can be used to map out the spatial distribution of the cluster gas. A detector with energy resolution, such as ACIS, can also measure the cluster spectrum as indicated in Figure 2.1. If the detector response is well-understood, the measured spectrum can be used to back out the best-fit electron temperature, elemental abundance, and X-ray cooling function of a cluster. These quantities can be combined with the spatial distribution of the gas to directly calculate the gas mass of a cluster. Other cosmologically interesting properties such as total gravitational mass and distance can also be inferred; see Chapter 5 for a detailed description of these methods.

2.2 The Sunyaev-Zel'dovich Effect in Clusters

Theoretical work on the SZE dates back to Sunyaev & Zel'dovich (1970), wherein the authors presented work on distortions of the CMB spectrum due to interactions of CMB photons with hot plasmas. This roughly coincided with the discovery of X-ray emission in galaxy clusters, and in Sunyaev & Zel'dovich (1972) the authors expanded their theoretical framework to include clusters of galaxies. Their prediction that inverse Compton scattering of CMB photons with hot cluster gas would give rise to an observable distortion in the CMB spectrum was seen as a way to independently verify the bremsstrahlung theory of X-ray emission. In practice detection of the SZE turned out to be more difficult than anticipated (e.g. Birkinshaw, 1991)

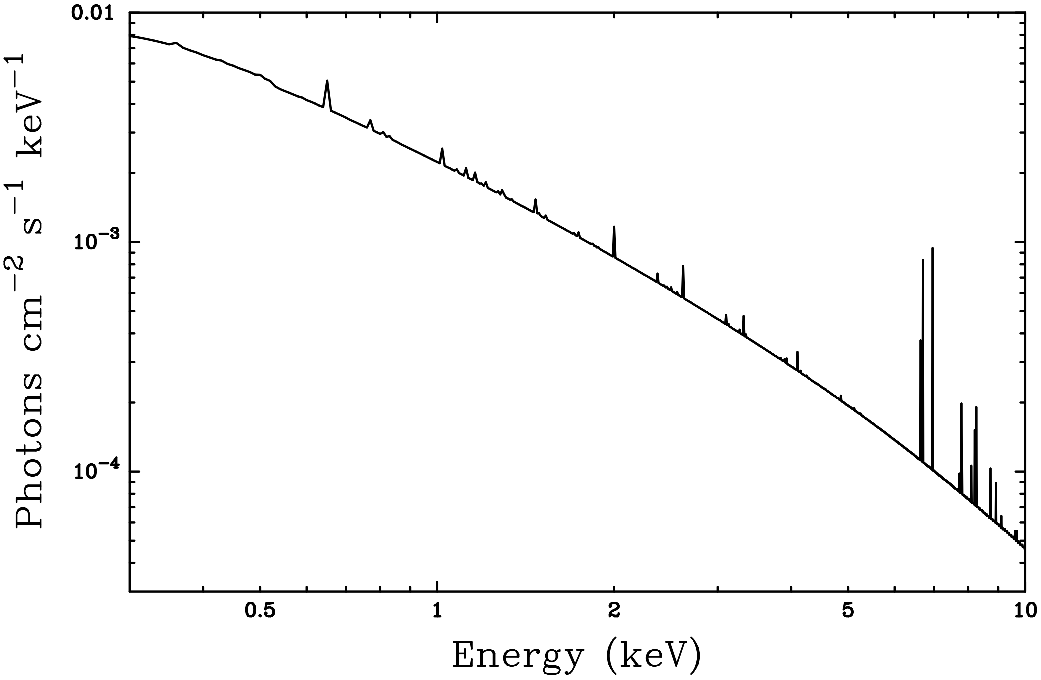

Figure 2.1: Raymond-Smith X-ray spectrum for a cluster with $kT_e = 10$ keV and abundance 30% of solar at $z = 0$.

and the bremsstrahlung theory was verified through X-ray studies alone. However, it was recognized early on that the SZE, when combined with X-ray data, could be used to measure the angular diameter distance D_{A} and subsequently the Hubble constant (Cavaliere et al., 1977; Silk & White, 1978; Birkinshaw, 1979), and there was a continuing effort to detect it.

2.2.1 SZE Theory

The thermal SZE is a small ($\lesssim$ 1 mK) distortion in the CMB spectrum caused by inverse Compton scattering of the CMB photons off of energetic electrons in the hot intracluster gas. In a typical massive cluster, a CMB photon passing through the center has a roughly 1% chance of scattering with an electron, and on average will achieve a fractional energy gain equal to $k_{\mathrm{B}}T_e/m_ec^2$. The spectral distortion is therefore proportional to the cluster optical depth $\tau = \int n_e \sigma_{\mathrm{T}} dl$ times the fractional energy gained per scatter, and can be expressed for dimensionless frequency $x \equiv h\nu / k_{\mathrm{B}} T_{\mathrm{CMB}}$ as a temperature change ΔT relative to the CMB temperature T_{CMB}:

$$\frac{\Delta T}{T_{\mathrm{CMB}}} = f(x) y = f(x) \int \sigma_{\mathrm{T}} n_e \frac{k_{\mathrm{B}} T_e}{m_e c^2} \, d\ell. \tag{2.4}$$

Here y is the Compton-y parameter, σ_{T} is the Thomson scattering cross-section of the electron, and $f(x)$ contains the frequency dependence of the SZE. The integral is along the line of sight. The frequency dependence can be expressed as

$$f(x) = \left(x \frac{e^x + 1}{e^x - 1} - 4 \right) (1 + \delta_{\mathrm{SZE}}(x, T_e)) \tag{2.5}$$

where $\delta_{\mathrm{SZE}}(x, T_e)$ is a relativistic correction to the frequency dependence. Electron velocities are relativistic at temperatures typical of the clusters considered in this work ($5 \lesssim T_e \lesssim 15$ keV), and many authors have worked out theoretical corrections for this effect (e.g., Rephaeli & Yankovitch, 1997; Stebbins, 1997; Itoh et al., 1998; Challinor & Lasenby, 1998; Sazonov & Sunyaev, 1998a,b). We ultimately adopt the corrections of Itoh et al. (1998) which are good to fifth order in $k_{\mathrm{B}} T_e / m_e c^2$. These corrections are analytic and easy to compute, and in general analytic and numerical treatments agree well below ~ 15 keV (Reese et al., 2002). More details of our analysis are presented in Chapter 5.

Two particularly interesting properties of the thermal SZE can be seen in Eq. [2.4]. First, it is really just the line of sight integral of the gas pressure, $P_{\mathrm{gas}} \propto n_e T_e$. Second, the thermal SZE is independent of redshift; although the CMB experiences cosmological dimming, the ratio $\frac{\Delta T}{T_{\mathrm{CMB}}}$ does not. This redshift independence makes the SZE an excellent probe of the high-z universe. The thermal SZE spectrum is shown as

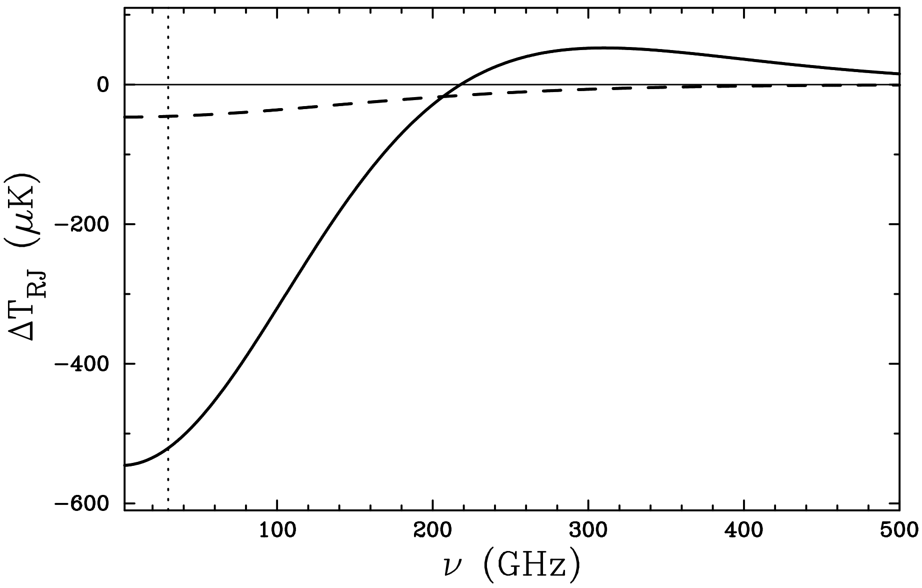

Figure 2.2: The Sunyaev-Zel'dovich Effect spectrum in units of the Rayleigh-Jeans brightness temperature. The heavy solid curve reprents the thermal SZE spectrum, and the dashed curve is the kinetic SZE spectrum. The dotted vertical line is drawn at 30 GHz, the frequency at which our observations are performed. The curves shown are for $y_c = 10^{-4}$ and $V_p = 1000$ km s^{-1}. Note that the peculiar velocity curve would be positive if V_p were negative (cluster moving toward us).

the heavy solid line in Figure 2.2. The spectrum is plotted in units of the Rayleigh-Jeans (RJ) brightness temperature ($T_{\rm RJ}$), the units in which radio telescopes are typically calibrated. The SZE can also be expressed in specific intensity units, more common in millimeter and submillimeter astronomy; see Carlstrom et al. (2002) for more on this distinction. Note that the SZE is a thermal decrement at low frequencies and an increment at high frequencies due to the upscattering of photons by the hot electrons. The zero-crossing occurs at $\sim$ 218 GHz, typically referred to as the thermal null.

In addition to the thermal effect, there is a kinetic SZE that arises from scattering of CMB photons in a cluster with line of sight motion, or peculiar velocity V_p, relative to the CMB rest frame. Such scattering gives rise to a Doppler shift which is seen as a distortion of the CMB spectrum, although the kinetic distortion is indistinguishable from primary CMB anisotropy. The kinetic SZE can be expressed as

$$\frac{\Delta T_{\mathrm{kin}}}{T_{\mathrm{CMB}}} = -\tau \frac{V_p}{c} \tag{2.6}$$

and is shown as a dashed line in Figure 2.2. As Eq. [2.6] indicates, the kinetic SZE is a negative distortion for positive V_p (cluster moving away from us) and vice versa. The thermal SZE generally dominates the kinetic effect by at least an order of magnitude. However, the kinetic SZE can be studied by instruments with frequency sensitivity near the thermal null, and recent studies have placed limits on cluster peculiar velocities using this method (Holzapfel et al., 1997a; Benson et al., 2003). The kinetic SZE is a potentially powerful method of probing large scale structure in the universe through deviations of cluster motion relative to the Hubble flow. However, given that it is a minor effect at our observing frequency of 30 GHz, it is not treated in this work.

A more detailed treatment of the derivation of the SZE and other theoretical details can be found in the reviews of Sunyaev & Zel'dovich (1980), Rephaeli (1995), and Birkinshaw (1999).

2.2.2 SZE Observations

The history and status of SZE observations are well-reviewed by Birkinshaw (1991), Birkinshaw (1999) and Carlstrom et al. (2002). Given the relative weakness of the SZE signal, controlling systematics such as ground pickup and atmospheric noise was the major early impediment to successfully detecting the SZE. The development of new instrumentation and observing strategies, however, has led to many high significance detections in the last decade. Single dish detections, which generally control systematics through the use of beam switching on leading and trailing fields, have been made using the OVRO 40 m telescope at 20 GHz (Birkinshaw et al., 1991; Birkinshaw & Hughes, 1994) and the OVRO 5.5 m telescope at 32 GHz (Herbig et al., 1995; Myers et al., 1997; Mason et al., 2001). Bolometric measurements using drift scan techniques have successfully mapped the SZE at millimeter wavelengths in a growing sample of clusters (Holzapfel et al., 1997b,a; Mauskopf et al., 2000a; Benson et al., 2003, 2004), and submillimeter measurements have also been reported (Lamarre et al., 1998; Komatsu et al., 1999; Gomez et al., 2004). Interferometers have also emerged as an excellent way of imaging the SZE due to their stability and spatial filtering capabilities (see §4.2.1 for more details). Detections from the BIMA/OVRO SZE imaging experiment at 30 GHz (Carlstrom et al., 1996; Grego et al., 2000; Reese et al., 2000; Grego et al., 2001; Joy et al., 2001; Reese et al., 2002; LaRoque et al., 2003) and the Ryle Telescope at 15 GHz (Grainge et al., 1993, 1996, 2002a,b; Saunders et al., 2003; Jones et al., 2005) have been reported in the last decade. Most recently, detections from both the Very Small Array (VSA) at 32 GHz (Lancaster et al., 2005) and the Cosmic Background Imager (CBI) between 26 and 36 GHz (Udomprasert et al., 2004) have been reported.

The future of SZE observations is promising as well. On the bolometer front, the BOLOCAM experiment (Mauskopf et al., 2000b) is now on-line in Hawaii, and construction of a new 1000-element millimeter and sub-millimeter bolometric array, the South Pole Telescope (SPT, Ruhl et al. 2004) has begun. The SPT is expected to detect the SZE toward thousands of clusters as part of an ambitious survey. Similar upcoming surveys that make use of bolometers include the Atacama Cosmology Telescope (ACT, Kosowsky 2003) and the Atacama Pathfinder Experiment (APEX, Schwan et al. 2003). Interferometric surveys are also in progress or about to begin, including the Sunyaev-Zel'dovich Array (SZA) (Carlstrom et al., 2002), the Arcminute MicroKelvin Imager (AMI) (Kneissl et al., 2001), and the Array for Microwave Background Anisotropy (AMiBA) (Lo et al., 2001). More information on SZE surveys and other applications of X-ray and SZE emission for cosmology is presented in the next section.

2.3 Cosmology with X-ray Emission and SZE

Current favored models of galaxy cluster formation hold that clusters collapse from volumes on the order (10 Mpc)^3 down to typical volumes of order (1 Mpc)^3; they have typical gravitational masses between 10^{14} and 10^{15} $M_\odot$, and, when in a sufficiently relaxed state, should obey the virial theorem, i.e., have total kinetic energy equal to one-half their potential energy. Roughly 10% of their total mass is baryonic, of which most is in the form of hot (3—10 keV) gas. Their sensitivity to gravitational physics on these scales makes clusters excellent probes of large scale structure and makes them useful for studying cosmological models. With both X-ray emission and the SZE now well-established observational signatures of the hot gas in clusters, we describe several ways in which these data can be used to study cosmology.

2.3.1 Ω_M and Ω_Λ From Cluster Gas Mass Fractions

Since galaxy clusters collapse from such large spatial scales, they are expected to contain baryons and dark matter in proportions similar to the universal values (White et al., 1993b; Evrard, 1997); the baryonic mass fraction $f_{\rm B}$ of a cluster should reflect the ratio Ω_B/Ω_M where Ω_M is the ratio of total matter density in the universe to the critical density needed to close the universe. Likewise, Ω_B is the ratio of total baryonic density to the critical density. Both X-ray emission and the SZE can be used to estimate $f_{\rm B}$ in clusters. With knowledge of the gas temperature, one can use either S_x or ΔT to solve for the central gas density and integrate over the gas distribution to determine $M_{\rm gas}$. The total mass $M_{\rm total}$ can be determined by assuming that the gas is in hydrostatic equilibrium (HSE) with the cluster potential. The gas mass fraction $f_{\rm gas}$ is then simply $M_{\rm gas}/M_{\rm total}$. Not all baryons reside in the gas; there is also a baryonic component in stars (e.g., White et al., 1993b; Kravtsov et al., 2005) and some hydrodynamical simulations show depletion of baryons during cluster formation (e.g., Evrard, 1997). Therefore the measured gas mass fraction provides a lower limit to the baryon fraction:

$$f_{\rm gas} \leq f_{\rm B} = \Omega_B/\Omega_M. \tag{2.7}$$

Measurements of Ω_B are available in the literature from D/H measurements combined with Big Bang nucleosynthesis (BBN) predictions (Copi et al., 1995; Burles & Tytler, 1998b,a; Nollett & Burles, 2000; O'Meara et al., 2001) and more recently from measurements of CMB anisotropy (Spergel et al., 2003). The cluster gas mass fraction then provides an upper limit to Ω_M:

$$\Omega_M \leq \Omega_B/f_{\rm gas}. \tag{2.8}$$

This method has been applied by many authors using X-ray data (e.g., Allen et al., 2002; Mohr et al., 1999; Ettori & Fabian, 1999; David et al., 1995; White et al., 1993b) and more recently with SZE data as well (LaRoque et al., 2004; Grego et al., 2001; Myers et al., 1997). The results of these studies consistently indicate $\Omega_M \lesssim 0.3$, consistent with measurements of cluster abundances (e.g., Bahcall & Fan, 1998) and the CMB (Spergel et al., 2003). This method can also test theories of cluster structure by examining the effect of different baryonic inventories on Ω_M and comparing with independent results. For instance, Grego et al. (2001) assume a baryonic mass component in galaxies equal to $0.20h^{3/2}M_{\rm gas}$, where h is defined such that H_0=100 h km s^{-1} Mpc^{-1}. They also assume that the total baryonic content of clusters is depleted by $\sim$15% relative to the universal value (Evrard, 1997) during cluster formation. Using these assumptions about cluster structure to convert $f_{\rm gas}$ to $f_{\rm B}$ and using Eq. [2.7], they obtain $\Omega_M \sim 0.25$, in good agreement with independent studies.

The dark energy density Ω_Λ can be measured by an extension of this method proposed by Sasaki (1996) and Pen (1997). They argue that since the gas mass fraction in clusters reflects Ω_B/Ω_M, and this ratio is generally assumed to be constant with redshift, the gas mass fraction should also be constant with redshift. They then make use of the fact that $D_{\rm A}$ must first be specified in order to deproject the X-ray surface brightness or SZE decrement to solve for $f_{\rm gas}$. Since $f_{\rm gas}$ depends on $D_{\rm A}$, and $D_{\rm A}$ depends on cosmology as demonstrated in Figure 2.3, the "correct" cosmology is taken to be the one that gives a flat $f_{\rm gas}$ versus z curve. This method is applied by Allen et al. (2002) and Allen et al. (2004), in which they use cluster X-ray data with priors on h and Ω_B to obtain non-zero limits on Ω_Λ.

This is a powerful method for testing cosmology since it assumes only that $f_{\rm gas}$ should be constant with redshift. Since the normalization of $f_{\rm gas}$ is not important, a precise understanding of the baryon budget in clusters is not necessary. However, as will be shown in Chapter 6, current X-ray and SZE data cannot yet place tight constraints on Ω_M and Ω_Λ using this method without priors on either the geometry of the universe or Ω_B. Given the state of the data, this method therefore works best in combination with the independent Ω_M constraints described above; together these two methods provide tests of both cosmology and cluster structure. The results of these tests using our 36 cluster sample are presented in §6.2.

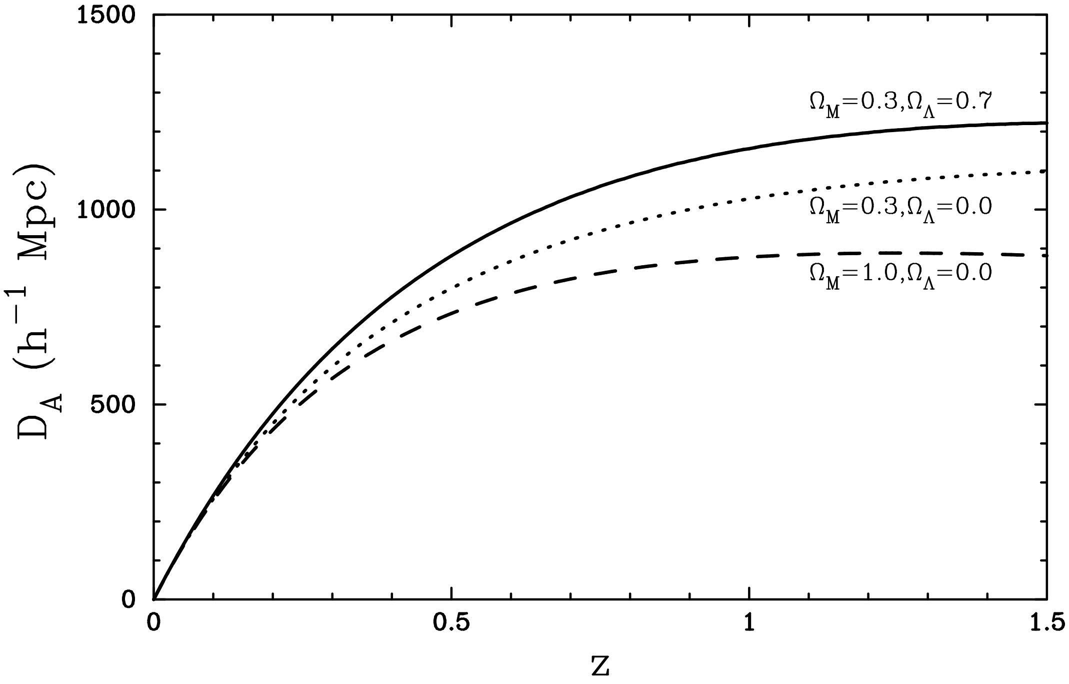

Figure 2.3: The angular diameter distance as a function of redshift for three representative cosmologies: a flat, Λ-dominated universe (solid line), a flat matter dominated universe (dashed line), and an open universe with no Λ (dotted line). At a given redshift, D_A increases as Ω_Λ is increased but decreases as Ω_M is increased.

2.3.2 Cluster Surveys

Tracing the abundance of clusters in the universe as a function of redshift is expected to provide strong constraints on cosmological parameters. The formation of cluster potential wells should depend mainly on the geometry of the universe and the power spectrum of initial density fluctuations, and be largely independent of complicated gas dynamics and feedback processes (e.g., Haiman et al., 2001). Cluster catalogs compiled from surveys at X-ray, optical, or radio wavelengths are therefore a valuable cosmological tool. The yields from cluster surveys are sensitive to a combination of two quantities: the volume element per unit solid angle as a function of redshift $dV/(dz\,d\Omega)$, and the number density of clusters as a function of mass and redshift, $dn(M,z)/dM$. The volume element depends on Ω_M and Ω_Λ through the angular diameter distance (Peebles, 1980). The function dn/dM can be derived from the statistics of peaks in a Gaussian random field (Press & Schechter, 1974; Sheth & Tormen, 1999) or determined using N-body simulations (Jenkins et al., 2001). The shape and normalization of dn/dM are sensitive to both the variance in the initial density field σ_8, and the linear growth function $D(z)$ which describes how the amplitude of the density field grows with time (Carroll et al., 1992). In general dn/dM decreases exponentially with mass on cluster mass scales, implying that very massive clusters are rare. The expected change in abundance as a function of redshift measured by a survey with well defined minimum detectable mass $M_{\min}$ is (Haiman et al., 2001):

$$\frac{dN}{dzd\Omega}(z) = \frac{dV}{dzd\Omega}(z) \int_{M_{\min}(z)}^{\infty} \frac{dn(M,z)}{dM}\, dM. \tag{2.9}$$

For a survey covering solid angle $d\Omega$, the shape and normalization of the dN/dz curve are very sensitive to Ω_M, Ω_Λ, σ_8, and even h through their dependence on the volume element, initial power spectrum, and linear growth function. The shape is also sensitive to the equation of state of the dark energy, w, where the dark energy density $\rho_{\rm DE}$ depends on the scale factor R as $\rho_{\rm DE} \propto R^{-3(1+w)}$. Throughout this work, dark energy is assumed to refer to a cosmological constant Λ, which is independent of R and therefore has $w = -1$. However, theories suggesting $w > -1$ or a redshift dependent w have been proposed (Turner & White, 1997; Caldwell et al., 1998) and dN/dz should be sensitive to the value of w since it affects both linear growth of fluctuations and the volume element (Haiman et al., 2001; Wang & Steinhardt, 1998). More detailed methods for constraining cosmological parameters through dN/dz can be found in the literature (e.g., Carlstrom et al., 2002; Haiman et al., 2001; Holder et al., 2001; Kneissl et al., 2001; Holder et al., 2000b; Mohr et al., 2000a).

In order to distinguish between cosmological models using the shape and normalization of the dN/dz curve, it is necessary to have a sample that extends to high redshift and has a well-understood selection function. An SZE survey should satisfy these conditions. The fundamental observable in such a survey is the integrated SZE flux, $S_{\rm SZE}$. This is essentially a temperature-weighted inventory of the total number of electrons in the cluster, which is trivially related to the gas mass:

$$S_{\rm SZE} = \int \Delta T \, d\Omega \propto \frac{M_{\rm gas} \langle T_e \rangle}{{D_{\rm A}}^2} \tag{2.10}$$

where $d\Omega$ is the solid angle of a cluster and goes as ${D_{\rm A}}^{-2}$. The flux measured for a cluster of a given mass has a very weak redshift dependence; $D_{\rm A}(z)$ flattens out at high-z as shown in Figure 2.3, and a cluster of given mass should be denser and therefore hotter at higher redshift since the density of the universe increases as $(1+z)^3$. An SZE survey with a given flux threshold should therefore have a well-defined limiting mass which is nearly independent of redshift. This makes SZE surveys an ideal tool for compiling cluster catalogs out to high-z and studying the dN/dz curve (Holder et al., 2000b).

X-ray surveys such as the *Einstein* Medium Sensitivity Survey and *ROSAT* Deep Cluster Survey have also been used to place constraints on cosmology through the abundance of low and moderate redshift clusters (e.g., Borgani et al., 2001; Bahcall & Fan, 1998; Donahue et al., 1998; Viana & Liddle, 1999), and more comprehensive X-ray surveys such as the *XMM* serendipitous survey (Romer et al., 2001) have been proposed. However, the X-ray selection function has a strong redshift dependence (e.g., Eq [2.3]) making it more difficult to trace dN/dz out to high-z, and in this work we focus only on SZE surveys.

2.3.3 The Hubble Constant

Since the SZE signal is proportional to the density integrated along the line of sight, while the X-ray signal goes as $\int n_e^2 dl$, the combination of the two can be used to solve for the line of sight size of the cluster by eliminating the density. This assumes knowledge of the temperature, which can be determined from X-ray spectra. For an assumed cluster geometry, one can then determine the angular diameter distance $D_{\rm A}$ to the cluster by comparing its actual size to its angular size. This distance, combined with redshift, can be used to determine the Hubble constant, H_0. This is a powerful method for measuring H_0 since it is independent of the cosmic distance ladder and does not assume that clusters are standard candles or standard rulers. It relies only on straightforward assumptions about cluster physics. Recent applications of this method are well-reviewed in Birkinshaw (1999) and Carlstrom et al. (2002). The largest cluster samples used to measure H_0 are those of Reese et al. (2002) and Jones et al. (2005), although a compilation of distances for the sample of clusters studied in this work will be presented soon (Bonamente et al., in preparation).

2.3.4 Potential Obstacles in Interpreting Cosmological Results

The cosmological tests described here all rely on certain assumptions about cluster properties. Here we describe some of the uncertainties that must be confronted in order to use X-ray and SZE data to do cosmology.

Cluster masses and distances are not directly observable quantities, and assumptions about cluster structure and evolution are generally made to infer mass and distance from observables such as S_x, ΔT, and spectroscopically measured temperature T_x. For instance, when deprojecting S_x or ΔT to get the cluster density, the cluster is often assumed to be a sphere or biaxial ellipsoid. The gas distribution is usually treated as smooth, and since the measured X-ray temperature T_x is weighted toward regions that emit the most photons, some assumption must be made to infer the true electron temperature T_e of the cluster. Inferring the total cluster mass from X-ray or SZE data alone requires the assumption of HSE, which may not always be satisfied in clusters. Any of these effects could bias the derived distances, masses, and gas mass fractions, and subsequently the cosmology inferred from them such as H_0, Ω_M, and Ω_Λ. The impact of these assumptions can be determined by carrying out the analysis on simulated data with precisely known properties; this is demonstrated in Chapter 5. In addition, comparison of SZE results with X-ray results is informative since the X-ray and SZE observables have different sensitivities to n_e and T_e. Such comparisons and their implications are examined in Chapter 6. Observational uncertainties may bias the results as well. Errors in decoupling the X-ray surface brightness from the cosmic and instrumental X-ray background would bias the measured S_x, and failure to account for undetected radio point sources in a cluster field could bias ΔT. The impact of these and other systematic uncertainties is examined in §6.3.

The cosmological constraints provided by SZE surveys are similarly affected by assumptions about cluster structure and evolution. The expected shapes and normalizations of the dN/dz curves are generally determined from simulation results (e.g., Holder et al., 2000b). These simulations tend to form regular, virialized objects over a large range of redshifts. If this picture is in error, the true shape and normalization of dN/dz will differ from expectations, biasing the inferred cosmological parameters.

One method of testing the reliability of survey results is to construct scaling relations between certain cluster properties. If clusters are indeed regular, virialized objects that form from background densities that scale with redshift as $\rho \propto (1+z)^3$, the virial theorem predicts that the gas temperature should scale with cluster mass and redshift as

$$T_e \propto M_{\rm total}^{2/3} E(z)^{2/3}, \tag{2.11}$$

where

$$E(z) \equiv [\Omega_M (1+z)^3 + (1 - \Omega_M - \Omega_\Lambda)(1+z)^2 + \Omega_\Lambda]^{1/2} \tag{2.12}$$

and accounts for our convention that quantities in the scaling relations are measured relative to the critical density $\rho_{\rm crit}$ needed to close the universe, which evolves according to $E(z)$ (see §5.4.1).

Comparing this with Eq. [2.10], we find:

$$S_{\rm SZE} \propto \begin{cases} f_{\rm gas}\, T_e^{5/2}\, E(z)^{-1} \\ f_{\rm gas}\, M_{\rm total}^{5/3}\, E(z)^{2/3}\,. \end{cases} \tag{2.13}$$

Recent X-ray observations have shown strong correlations between cluster properties such as size, mass, temperature, and luminosity (e.g., Mohr & Evrard, 1997; Eke et al., 1998b; Mohr et al., 2000b; Finoguenov et al., 2001). Since SZE surveys will measure the integrated SZE flux, it is desireable to construct scaling relations such as those of Eq. [2.13] and study their slopes, scatters and normalizations to determine whether a firm connection can be made between observables such as integrated SZE flux and cosmologically significant cluster properties such as total mass. Comparison of the measured slopes and normalizations of these scaling relations with predictions from simulations helps us assess our understanding of cluster physics, while the scatter in the data helps us assess the regularity of clusters. We consider three scaling relations of particular interest to understanding cluster survey yields. We start with the $S_{\rm SZE}$-$M_{\rm gas}$ relation, which compares two quantities that should directly probe the intracluster gas distribution with little dependence on T_x or assumptions about cluster structure. This relation is therefore expected to show tight correlation; significant scatter would indicate a problem with our measurements or our understanding of cluster physics. The $S_{\rm SZE}$-T_x relation is of interest since T_x is generally assumed equal to T_e in determining $M_{\rm total}$ from HSE, though recent studies indicate that this may not be the case (Mazzotta et al., 2004; Rasia et al., 2005). Finally, the $S_{\rm SZE}$-$M_{\rm total}$ relation is significant since understanding the total masses of clusters detected in SZE surveys is critical to properly interpreting dN/dz. These scaling relations, constructed from our 36 cluster sample, are presented in §6.1 along with their implications for interpreting SZE survey yields.

CHAPTER 3

SAMPLE

To perform the cosmological tests described in Chapter 2, one would ideally have a sample satisfying three general conditions. First, the sample should be large enough that statistical uncertainties, which generally go as square root of the sample size n, are small compared to systematic uncertainties. Based on results from works similar to this one (e.g., Grego et al., 2001; Reese et al., 2002) and our current understanding of systematics, a sample size $n \gtrsim 10$ is ideal. Second, the sample should be selected in such a way as to avoid biasing it toward certain types of clusters, such as highly elongated ones or those undergoing significant merging activity. Such selection effects and their impact on cosmological results will be discussed further in this section and in Chapter 6. Finally, the sample should cover a large range in redshift, ideally extending to at least $z \sim 0.5$. This choice is made based on both the behavior of the $D_{\rm A}$-z curve (Figure 2.3), which shows that different cosmologies are easier to distinguish at high redshifts, and the logistical constraint that the current catalog of X-ray and SZE detected clusters thins rapidly beyond $z \sim 0.5$.

In this section we describe the steps involved in compiling our cluster sample. We start with basic observational selection criteria and discuss some of the major associated selection effects. We then describe properties of the specific X-ray catalogs from which clusters in our sample are drawn. Finally we present our 36 cluster sample, which largely satisfies the three conditions set out above.

3.1 Observational Selection Criteria

Our sample consists of clusters that have both *Chandra* X-ray data and SZE data from the BIMA/OVRO SZE imaging project, which uses the Berkeley-Illinois-Maryland

Association (BIMA) and Owens Valley Radio Observatory (OVRO) centimeter-wave interferometers to image the SZE. Since SZE detection systems have only recently become fast enough to efficiently perform blind surveys (cf. §2.2.2), early SZE observations were targeted toward clusters with previous X-ray detections. X-ray surveys have historically provided particularly reliable cluster detections. Since X-ray surface brightness is sensitive to n_e^2, the probability of a line of sight superposition of two smaller objects being mistaken for a single massive cluster is extremely small. Many optically selected cluster catalogs exist (e.g., Abell, 1958; Zwicky et al., 1961) but are more prone to projection effects. Furthermore, the detection of X-ray emission from a cluster indicates that it has an gaseous intracluster medium (ICM) and may therefore have a detectable SZE; this is not the case for optical detections. The BIMA/OVRO SZE imaging project has generally pursued hot clusters (published $T_x \gtrsim 5$ keV) which by inference should be massive and have a stronger SZE (Grego, 1999; Reese, 2001). Hot clusters are also expected to have gas mass fractions more closely resembling the universal value (Mohr et al., 1999).

Several observational constraints exist in selecting clusters to observe from BIMA and OVRO. Since OVRO is at 37° latitude and BIMA is at 41°, the minimum observable declination is $\sim -15°$. The properties of the instruments themselves also impose observational limitations. Interferometers simultaneously measure a limited range of angular scales, imposed by the projected separations (baselines) of the telescope dishes relative to the source (cf. §4.2.1). An interferometer therefore cannot detect a cluster that subtends too large an angle on the sky, since the minimum projected baseline is limited by the finite size of the dishes. For typical physical cluster sizes of ~ 1 Mpc, BIMA and OVRO are limited to redshifts $z \gtrsim 0.15$. Another observational limitation involves radio point sources. The sensitivity of the interferometer to a range of angular scales allows point sources to be simultaneously detected and later removed from cluster data. The greatest point source sensitivity comes from the longest baselines, but longer baselines have poorer associated phase stability. The ability to accurately decouple the point source flux from the cluster signal therefore depends on the phase stability of the interferometer. The present system is capable of removing point sources with beam attenuated fluxes $\lesssim 20$ mJy (Reese, 2001); clusters containing point sources with higher beam attenuated fluxes are not observed.

3.1.1 Selection Effects

Another property used in selecting clusters to pursue in SZE is X-ray luminosity, L_x. X-ray survey catalogs typically include all clusters with fluxes above a certain threshold, but selecting on the basis of flux may introduce a bias. For instance, a prolate cluster (biaxial ellipsoid with long axis of symmetry) whose intrinsic luminosity would correspond to a measured flux near the survey limit will be detected if its symmetry axis is aligned with the line of sight, but missed if its symmetry axis is in the plane of the sky. Selecting by flux would therefore bias the SZE sample toward clusters elongated along the line of sight, and applying a spherical model to the ICM distribution would ultimately bias the derived cosmological parameters. Selecting by luminosity instead of flux alleviates this problem, although it may introduce other biases. For instance, highly relaxed clusters have dense, cool cores which, because of the $n_e^2 T_e^{1/2}$ dependence of cluster X-ray emission, have high associated luminosities; these "cool-core" clusters are discussed in §5.1.2. Some clusters undergoing major mergers are also expected to have very high luminosities. Such clusters may be preferentially chosen when selecting by luminosity.

Another selection effect involves our exclusion of clusters with bright radio point sources. A correlation exists between cool-core clusters and radio point sources

(Burns, 1990; Peres et al., 1998) so choosing clusters in this way may select against cool-core clusters. In addition, point source flux falls off with distance squared whereas the SZE is redshift independent; our sample might therefore be biased toward high-z clusters, whose properties might differ from those of nearby clusters.

The potential impact of these selection effects on derived cluster properties and cosmology will be discussed in §6.3.

3.2 X-ray Cluster Catalogs

Nearly all clusters in our final X-ray/SZE sample come from at least one of four large X-ray catalogs. Each of these is briefly reviewed.

The *Einstein Observatory* Extended Medium-sensitivity Survey (EMSS, Gioia et al., 1990) is a serendipitous survey covering 778 square degrees away from the galactic plane ($|b| > 20°$). The sample consists of both Galactic and extra-galactic sources, including primarily AGNs, stars, and galaxy clusters. Exposure times varied according to field resulting in limiting fluxes that range from $\sim 5 \times 10^{-14}$ to $\sim 3 \times 10^{-12}$ erg cm^{-2} s^{-1} in the 0.3—3.5 keV energy band. Although it lacks a well-defined limiting flux, the catalog extends to $z > 0.8$ and it has proved to be a valuable source for studies which constrain cosmology through structure formation models (e.g., Henry et al., 1992; Bahcall & Fan, 1998; Donahue et al., 1998, 1999). Several of the highest redshift clusters in our SZE sample are drawn from this catalog.

The X-ray Brightest Abell-type Clusters catalog (XBACs, Ebeling et al., 1996b,a) is one of several surveys based on data from the serendipitous *ROSAT* All Sky Survey (RASS) (Voges, 1992). XBACs performs a cross correlation between extended sources in the RASS and clusters in the optical catalog of Abell, Corwin, & Olowin (1989) (ACO) to compile an X-ray catalog of 242 Abell-type clusters at high Galactic latitudes ($|b| > 20°$). The catalog has a limiting flux of 5.0×10^{-12} erg cm^{-2} s^{-1} in the 0.1—2.4 keV band and is generally restricted to $z \leq 0.2$; 24 clusters at $z > 0.2$ are included since they meet the flux requirement, but are not considered part of the statistical sample. Although it is shallower than the EMSS, it covers a much greater fraction of the sky and has a well-defined flux limit. Because of its relatively high limiting flux, clusters at $z \gtrsim 0.15$ have high X-ray luminosities and are therefore expected to be hot, making them ideal for SZE observations. Furthermore, the cross-correlation with the well-known ACO catalog means that many of the clusters detected are well-studied, which may help to quantify systematic effects.

The *ROSAT* Brightest Cluster Sample (BCS, Ebeling et al., 1998) is also based on the RASS, but searches the entire northern hemisphere at high Galactic latitude ($|b| > 20°$); it looks for extended X-ray emission at the positions of both Abell and Zwicky clusters but also flags bright, extended X-ray sources from the RASS and performs optical follow-up observations to determine whether these sources are clusters. Unlike XBACs, it is therefore an X-ray selected sample rather than optically selected. Its properties are otherwise similar to XBACs; it has a slightly lower limiting flux, 4.4×10^{-12} erg cm^{-2} s^{-1}, and extends to higher redshift ($z \leq 0.3$), but is still expected to detect mainly hot, X-ray luminous clusters at $z \gtrsim 0.15$ that are ideal for SZE observations.

The Massive Cluster Survey (MACS, Ebeling et al., 2001a) combines the largest solid angle of any RASS-based survey ($22,735$ deg^2) with a relatively low X-ray flux limit (1×10^{-12} erg cm^{-2} s^{-1}) to maximize the number of cluster detections at redshifts $z > 0.3$. The survey has already discovered more than 100 clusters at redshifts $0.3 \lesssim z \lesssim 0.7$, providing an independent test of the EMSS results. Like the BCS, it is an X-ray selected sample; it applies a flux cut and hardness ratio cut to the 18,811 X-ray sources in the RASS Bright Source Catalog (Voges et al., 1999) in an effort to isolate those objects which may be distant clusters. MACS avoids the Galactic plane ($|b| > 20°$) and is limited to declinations between $-40°$ and $80°$, since spectroscopic follow-up from Mauna Kea is performed on all suspected clusters in order to obtain redshifts. Its sensitivity at high-z makes MACS, like the EMSS, a powerful tool for cosmological tests. However, its limiting flux is generally higher than that of EMSS, meaning that only extremely luminous (and by inference, highly massive) clusters will be selected at high redshifts. As indicated in §3.1.1 such extreme clusters may have unusual properties, and the implications of this selection effect will be discussed in §6.3.

3.3 Final Cluster Sample

Two additional cuts are made in compiling the final X-ray/SZE cluster sample: the selected clusters must have publicly available *Chandra* data as of 2004 October, and it must be possible to fit an isothermal β-model to the X-ray surface brightness profiles (see §5.1.1 for a detailed description of this model). The first criterion is easily satisfied, as the *Chandra* archive now contains several hundred galaxy clusters. The second criterion is more stringent as a cluster must have a smooth gas distribution with a characteristic shape in order to be well-fit by the β-model. Several clusters were rejected due to their highly irregular morphologies, evidence of strong merging activity. Note that this could partially offset the luminosity-based selection bias discussed in §3.1.1. In addition, the inner 100 kpc of each cluster is masked out from the X-ray data during model fitting in order to reduce systematics associated with cluster cores (cf. §5.4). Two clusters no longer had sufficient source counts after core removal for the β-model to converge, and were excluded from the final sample.

The final cluster sample is shown in Table 3.1. This is the only place that the full cluster names appear; abbreviations are used in the remainder of this work. Redshifts and best-fit central SZE positions are also listed in Table 3.1. The SZE positions are chosen rather than the X-ray positions since X-ray data, with its n_e^2 dependence, is more sensitive to substructure. The SZE profile is proportional to the gas pressure integrated along the line of sight, and cluster pressure profiles are usually smooth (e.g., Markevitch et al., 2000, 2001).

The X-ray 2—10 keV luminosities are also calculated for these clusters using the archived *Chandra* data and are included in Table 3.1. Many of our clusters have published luminosities in the catalogs described in the last section; however, we consider only the *Chandra* values in the remainder of this work since they are self-consistent, and in general result from longer, pointed exposures and therefore have less uncertainty.

Most Abell clusters are drawn from the BCS or XBACs, as are Zw3146 and R2129 which come from the BCS. Clusters beginning with "MS" are drawn from the EMSS, as is CL0016. Many clusters are listed in more than one catalog; for instance, CL0016 and MS0451 also appear in the MACS catalog and there is considerable overlap between the BCS and XBACs. Some clusters are not part of these catalogs but were observed in SZE for other reasons. A370 was the first cluster found to contain a strongly gravitationally lensed arc (Soucail et al., 1988); the arc properties indicated a high mass for this cluster. A611 is part of the extended BCS (Ebeling et al., 2000), a low-flux extension of the original catalog. CL1226 was discovered in the Wide-Angle *ROSAT* Pointed Survey (WARPS) (Scharf et al., 1997), a low-flux limit, small solid angle survey designed to identify clusters at very high redshifts in RASS data. At the time of its discovery, CL1226 was the most distant X-ray luminous cluster known (Ebeling et al., 2001b). R1347 is the most X-ray luminous galaxy cluster known (Schindler et al., 1997), while A1995 was identified as a distant bright

X-ray source in an early HEAO-1 survey (Kowalski et al., 1984) and also appears in the MACS catalog as MACS J1452.9+5802. Finally, the high-z cluster R1716 was discovered in the *ROSAT* North Ecliptic Pole Survey, a part of the RASS (Henry et al., 1997). It has since been included in the Bright Serendipitous High-redshift Archival Cluster (SHARC) catalog (Nichol et al., 1999), another survey optimized to detect very distant clusters in RASS data.

Altogether, the list in Table 3.1 constitutes a statistically large sample covering a wide range in redshift, $0.14 \leq z \leq 0.89$. While it is not necessarily free of selection bias, the clusters are generally drawn from surveys with well-understood selection functions. We should therefore be able to assess the level of bias that may be introduced.

Table 3.1. Cluster Sample

Cluster	z	Central SZ Position (J2000.0) (hh mm ss)	Central SZ Position (J2000.0) (dd mm ss)	L_x [a] (10^{45} erg s^{-1})	z reference
CL 0016+1609	0.541	00 18 33.3	16 26 04.0	1.87	Stocke et al. (1991)
Abell 68	0.255	00 37 04.0	09 10 02.5	0.73	Struble & Rood (1999)
Abell 267	0.230	01 52 42.3	01 00 26.0	0.37	Struble & Rood (1999)
Abell 370	0.375	02 39 52.4	−01 34 43.8	0.70	Struble & Rood (1999)
MS 0451.6−0305	0.550	04 54 11.6	−03 01 01.3	1.90	Gioia & Luppino (1994)
MACS J0647.7+7015	0.584	06 47 50.2	70 14 56.1	1.59	LaRoque et al. (2003)
Abell 586	0.171	07 32 19.6	31 38 55.3	0.31	Struble & Rood (1999)
MACS J0744.9+3927	0.686	07 44 52.4	39 27 33.2	1.53	LaRoque et al. (2003)
Abell 611	0.288	08 00 56.5	36 03 22.9	0.48	Struble & Rood (1999)
Abell 665	0.182	08 30 58.6	65 50 49.8	0.74	Struble & Rood (1999)
Abell 697	0.282	08 42 57.8	36 21 54.5	1.46	Struble & Rood (1999)
Abell 773	0.217	09 17 53.5	51 43 49.8	0.66	Struble & Rood (1999)
ZwCl 3146	0.291	10 23 37.8	04 11 17.8	1.21	Allen et al. (1992)
MACS J1115+53	0.458	11 15 14.7	53 20 09.9	1.07	Ebeling et al., in prep
MS 1137.5+6625	0.784	11 40 23.1	66 08 05.3	0.33	Donahue et al. (1999)
MACS J1149.5+2223	0.544	11 49 34.9	22 23 54.8	2.03	LaRoque et al. (2003)
Abell 1413	0.142	11 55 17.7	23 24 39.5	0.52	Struble & Rood (1999)

Table 3.1—Continued

Cluster	z	Central SZ Position (J2000.0) (hh mm ss)	(dd mm ss)	L_x[a] (10^{45} erg s^{-1})	z reference
CL 1226.9+3332	0.890	12 26.58.0	33.32 57.9	1.59	Ebeling et al. (2001b)
Abell 1689	0.183	13 11 29.1	−01 20 29.7	1.06	Struble & Rood (1999)
RX J1347.5−1145	0.451	13 47 30.6	−11 45 12.3	3.15	Schindler et al. (1995)
MS 1358.4+6245	0.327	13 59 50.2	62 31 07.0	0.51	Gioia & Luppino (1994)
Abell 1835	0.252	14 01 01.8	02 52 45.6	1.59	Struble & Rood (1999)
MACS J1423.8+2404	0.545	14 23 47.7	24 04 37.3	0.73	LaRoque et al. (2003)
Abell 1914	0.171	14 26 01.3	37 49 38.6	1.06	Struble & Rood (1999)
Abell 1995	0.322	14 52 58.1	58 02 57.0	0.63	Patel et al. (2000)
Abell 2111	0.229	15 39 40.2	34 25 00.4	0.40	Struble & Rood (1999)
Abell 2163	0.202	16 15 43.6	−06 08 46.6	2.28	Struble & Rood (1999)
Abell 2218	0.176	16 35 48.7	66 12 28.1	0.44	Struble & Rood (1999)
RX J1716.6+6708	0.813	17 16 51.2	67 07 49.6	0.42	Henry et al. (1997)
Abell 2259	0.164	17 20 09.0	27 40 09.4	0.24	Struble & Rood (1999)
Abell 2261	0.224	17 22 26.9	32 07 59.9	0.67	Struble & Rood (1999)
MS 2053.7−0449	0.583	20 56 21.0	−04 37 47.2	0.13	Stocke et al. (1991)
MACS J2129.4−0741	0.570	21 29 24.9	−07 41 43.9	1.29	LaRoque et al. (2003)
RX J2129.3+0005	0.235	21 29 38.1	00 05 12.4	0.58	Ebeling et al. (1998)

Table 3.1—Continued

Cluster	z	Central SZ Position (J2000.0) (hh mm ss)	(dd mm ss)	L_x[a] (10^{45} erg s^{-1})	z reference
MACS J2214.9−1359	0.450	22 14 58.4	−14 00 10.9	1.09	Ebeling et al., in prep
MACS J2228.5+2036	0.412	22 28 33.1	20 37 14.2	1.22	Böhringer et al. (2000)

[a]Calculated using flat cosmology with Ω_Λ=0.73, $h = 0.7$ over 2—10 keV frequency band.

CHAPTER 4

DATA

Data for the 36 cluster sample includes both archival *Chandra* data and 30 GHz SZE data collected at the BIMA and OVRO interferometric arrays. Table 4.1 shows the total good observing time for the sample for both X-ray (in ks) and SZE (in hrs). Periods of poor observing for which data were rejected are not included in the table. Here we describe the X-ray and SZE instruments, observations, and data reduction.

Table 4.1. Cluster Data

Cluster	*Chandra* X-ray Data ObsID	Chip	Exposure (ks)	Interferometric SZE Data BIMA (hr)	OVRO (hr)
CL0016	520	I3	67.4	43	100
A68	3250	I3	10.0	54	···
A267	1448	I3	7.4	50	···
A370	515	S3	65.3	26	33
MS0451	902	S3	42.2	···	30
MC0647	3196	I3	19.3	···	23
	3584	I3	20.0	···	···
A586	530	I3	10.0	45	···
MC0744	3197	I3	20.2	8	17
	3585	I3	19.4	···	···
A611	3194	S3	36.1	···	57
A665	531	I3	9.0	52	16
	3586	I3	29.7	···	···
A697	4217	I3	19.5	···	47
A773	533	I3	11.3	26	66
	3588	I3	9.4	···	···
Zw3146	909	I3	46.0	25	15
MC1115	3253	I3	8.8	···	15

Table 4.1—Continued

	Chandra X-ray Data			Interferometric SZE Data	
Cluster	ObsID	Chip	Exposure (ks)	BIMA (hr)	OVRO (hr)
MS1137	536	I3	77.0	88	...
MC1149	1656	I3	18.5	39	...
	3589	I3	20.0	...	...
A1413	537	I3	9.6	28	...
	1661	I3	9.7	...	...
CL1226	3180	I3	31.7	33	...
A1689	540	I3	10.3	16	26
	1663	I3	10.7	...	...
R1347	3592	I3	57.7	22	3
MS1358	516	S3	48.1	70	...
A1835	495	S3	19.5	27	23
	496	S3	10.7	...	...
MC1423	4195	S3	115.6	35	...
A1914	542	I3	8.1	24	...
	3593	I3	18.9	...	...
A1995	906	S3	56.7	50	58
A2111	544	I3	10.3	36	...
A2163	1653	I1	71.1	23	37

Table 4.1—Continued

	Chandra X-ray Data			Interferometric SZE Data	
Cluster	ObsID	Chip	Exposure (ks)	BIMA (hr)	OVRO (hr)
A2218	1666	I0	41.7	32	70
R1716	548	I3	51.7	37	...
A2259	3245	I3	10.0	25	...
A2261	550	I3	9.1	23	40
MS2053	551	I3	44.3	...	154
	1667	I3	44.5	...	...
MC2129	3199	I3	8.5	...	24
	3595	I3	18.4	...	...
R2129	552	I3	10.0	47	...
MC2214	3259	I3	19.5	41	11
	5011	I3	16.1	...	...
MC2228	3285	I3	19.9	39	...

4.1 *Chandra* X-ray Data

The *Chandra X-ray Observatory*, the third of NASA's so-called "Great Observatories," was launched in July 1999 as the U.S. follow-up to the *Einstein Observatory*. The *Chandra* spacecraft contains a high resolution mirror assembly, two X-ray imaging detectors, and two sets of transmission gratings for X-ray spectral studies. *Chandra*'s mirrors provide spatial resolution as low as $0''.5$, an order of magnitude better than those of both *Einstein* and *ROSAT*, and its ability to provide spectral information for each image pixel is an improvement over those missions as well. Although *Chandra*'s highest focused energy is not as high as that of *ASCA* (10 keV and 12 keV, respectively), *ASCA*'s mirror assembly limited it to $\sim 2'$ spatial resolution. A general description of the *Chandra* mission and its instruments can be found at the *Chandra* X-ray Center (CXC) homepage, `http://cxc.harvard.edu`, while Weisskopf et al. (2002) also give a good overview of the telescope and its main science goals. A highly detailed account of the instrument is contained in the *Chandra* Proposers' Observatory Guide at `http://cxc.harvard.edu/proposer/POG`; we give a brief overview of the instrument here to help put our data analysis methods in context.

4.1.1 Instrument

The *Chandra* observatory consists of a High Resolution Mirror Assembly (HRMA) with two focal plane detectors: a High Resolution Camera (HRC) and the Advanced CCD Imaging Spectrometer (ACIS). It also has two transmission grating spectrometers, the Low Energy Transmission Grating (LETG) and High Energy Transmission Grating (HETG) which can be used with either ACIS or the HRC to record data. Only the ACIS detector is used in this study of galaxy clusters, and neither the HRC nor the transmission gratings are discussed further.

The HRMA consists of four pairs of concentric grazing incidence mirrors and their support components. The focal length of the mirror assembly is 10.1 m and it has an unobscured clear aperture of 1145 cm^2. The mirrors have a thin iridium coating to improve X-ray reflectivity, but the mirror effective area drops precipitously from 800 cm^2 to 300 cm^2 at 2.1 keV due to an iridium absorption edge. The effective area then rises gradually to 400 cm^2 around 4.0 keV, but drops below 100 cm^2 beyond 8.0 keV. The FWHM of the point spread function (PSF) is $0''.5$ in conjunction with the detectors.

The ACIS detector consists of 10 planar, 1024×1024 pixel CCD's and has the ability to simultaneously perform high-resolution imaging and moderate resolution spectroscopy. The ten CCD's are divided into two arrangements: a 2×2 array used exclusively for imaging (ACIS-I) and a linear array of 6 CCD's which can be used either for imaging or as a readout for the transmission gratings (ACIS-S). The CCD

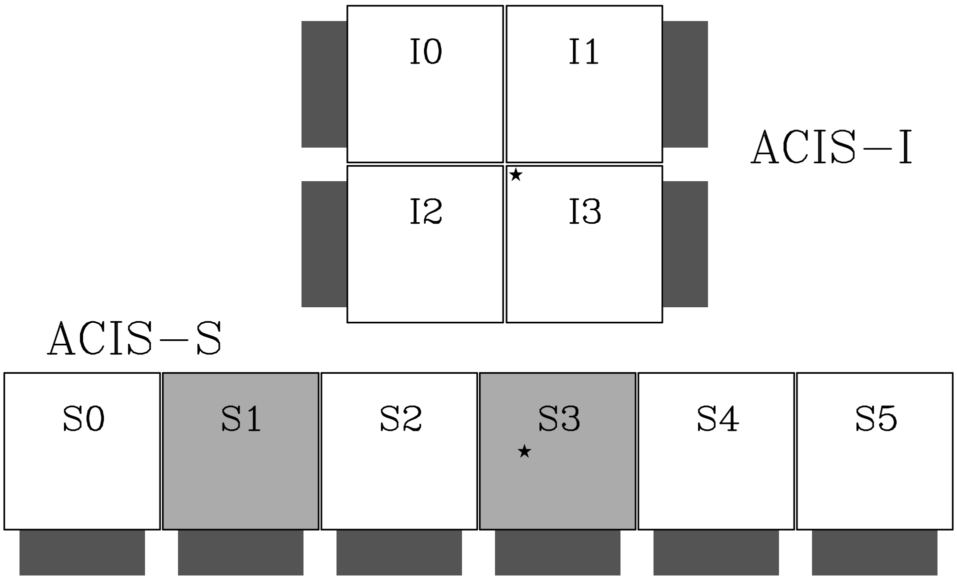

Figure 4.1: Schematic of the ACIS detector layout in the HRMA focal plane. The back illuminated chips S1 and S3 are shaded gray, all other chips are front-illuminated. The ACIS-I and ACIS-S aimpoints are marked by black stars. The dark grey bars show the positions of the detector readouts.

layout is shown in Figure 4.1. The ACIS pixels are 24 μm on a side, corresponding to $0''.492$ on the sky. This means that the spatial resolution for on-axis imaging with ACIS is limited by the physical size of the CCD pixels and not the PSF of the HRMA. This eliminates the need to do time-consuming convolutions of the model with the PSF in our data analysis.

The ACIS CCDs are composed primarily of silicon, with an active region on one side where most photon absorption takes place. Each absorbed photon liberates a proportional number of electrons, with an average of one electron liberated for every 3.7 eV absorbed. In a typical sequence, the active region is exposed for $\sim$ 3.2 s, after which the freed charge is transferred into a storage region in the chip. During the next exposure, the stored charge is transferred to a readout by alternating voltages, and the position and amplitude of each "event" are recorded. Each chip has four nodes, each containing its own charge transfer electronics and readout so that if one node